IEEE Access
Multidisciplinary ⋮ Rapid Review ⋮ Open Access Journal

Received January 26, 2022, accepted March 2, 2022, date of publication March 8, 2022, date of current version March 14, 2022.

Digital Object Identifier 10.1109/ACCESS.2022.3157311

Sliding Mode Control for Grid Integration of Wind Power System Based on Direct Drive PMSG

AHMED M. OSMAN, (Graduate Student Member, IEEE), AND FAHAD ALSOKHIRY, (Senior Member, IEEE)

Department of Electrical and Computer Engineering, Faculty of Engineering, King Abdulaziz University, Jeddah 21589, Saudi Arabia

Corresponding author: Ahmed M. Osman (amohammedsalimohammedosma@stu.kau.edu.sa)

This work was supported by the Deputyship for Research and Innovation, the Ministry of Education in Saudi Arabia, under Project 1071.

ABSTRACT Wind energy is predicted to account for a higher share of the world's total power generation in the future. However, as wind power becomes more prevalent in the grid, it poses new challenges in terms of grid reliability and stability. This opens up new possibilities for the development of control methods capable of supporting the grid during voltage disruptions as well as enhancing power quality issues. This paper proposes a sliding mode control scheme for a direct-drive PMSG based wind energy conversion system. Nonlinear Sliding Mode Control (SMC) has the merit of robustness and good disturbance rejection capability, making it effective in responding to grid disturbances. The SMC chattering effect, on the other hand, increases the overall harmonic distortion injected into the grid. In this paper, the demerit of SMC has been minimized with the proper selection of SMC reaching law and the inclusion of an LCL filter and its dynamics in the design of the SMC control law. Moreover, MATLAB/Simulink simulation results have shown that the proposed control strategy has a better performance than the optimally tuned proportional-integral control during grid voltage disturbances.

INDEX TERMS Grid-side converter control, machine-side converter control, permanent magnet synchronous generator, sliding mode control, wind energy.

I. INTRODUCTION

Renewable energy sources have aroused attention over the years as a viable source of electricity generation with low environmental impact [1]–[3], owing to growing concerns about future energy shortages and pollution. Due to the unlimited availability of wind energy, wind energy systems have expanded faster than any other energy source [4]. Globally, the installed capacity of wind power has been increased rapidly due to the aforementioned advantages and the reduction in costs. According to the latest data of the International Renewable Energy Agency (IRENA), the global installed capacity of wind power has been quadrupled in the last decade, from 180 GW in 2010 to 732 GW in 2020 as shown in Fig. 1 [5].

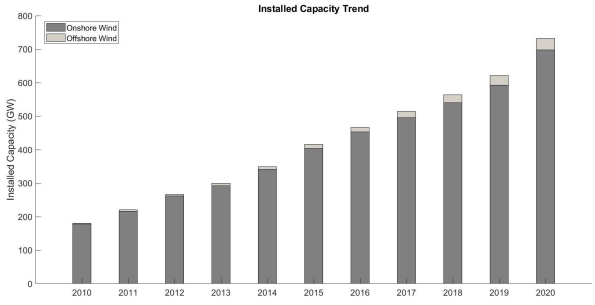

FIGURE 1. Installed capacity of wind turbines globally.

Generally, wind energy systems use three types of generators: doubly fed induction generator (DFIG), permanent magnet synchronous generator (PMSG), and induction generator. However, PMSG is a preferable choice for wind application for many reasons: it has higher efficiency, has a simple structure, can be connected directly to the turbine without a gearbox, and can easily extract the maximum wind power [6]–[8]. Moreover, the existence of a gearbox, which connects the wind turbine to the generator, presents technical and economic issues such as it may flaw and increase the cost of the wind turbine system. This requires frequent maintenance and condition monitoring to avoid these consequences [9]. Since it is more reliable, efficient, and produces

The associate editor coordinating the review of this manuscript and approving it for publication was Alfeu J. Sguarezi Filho.

less noise, direct-drive permanent magnet synchronous generators are considered a viable alternative [10]. Variable-speed functioning of the wind-turbine generator is required to capture the maximum energy from the fluctuating wind; thus, precise control is required for optimal power efficiency over a wide range of wind speeds [11]–[13].

The PI control law, which gives the simplest, and most practical solution to control issues, is still used today by most industrial controllers [14], [15]. However, parametric tuning of the PI controller is one of the most critical tasks performed during the testing of the control system to achieve the desired control responsiveness and performance [16]. Ref [17] provided a detailed analysis for the optimal tuning of PI controllers of a direct-driven PMSG connected to the grid using moduls optimum and symmetric optimum methods. Evolutionary optimization algorithms are also used for the PI control design. In [18], particle swarm optimization is used to tune the PI parameters of a grid-connected PMSG-based wind turbine with the objective function of minimizing the real part of the system's dominant pole. However, the linear control has many limitations; the optimal tuning of the PI controllers is not a straightforward task when it comes to the nonlinear systems that may encounter several operational points [19].

Several publications have been reported in the literature utilizing sliding mode control to control the converters of wind energy systems. A sliding mode control technique with Extend State Observer (ESO) is proposed in [20] for an offshore wind energy system. The ESO is used to enhance the maximum power extraction capability of the wind turbine by estimating the aerodynamic torque. Authors in [21] developed an MPPT – based optimal torque control strategy using a first-order integral sliding mode control. Results showed that the proposed SMC scheme has a better performance compared to the classical PI control. In [22] a complementary sliding mode control scheme is proposed for a two-mass model of a variable-speed wind turbine with the main aim of mitigating drive train oscillations. The authors of this article also compared the performance of different control strategies in terms of the MPPT's efficiency; the proposed scheme has higher electrical and aerodynamic efficiency when compared to the conventional SCM. The study in [23] suggests a robust sliding mode control strategy for a 1.5 MW variable-speed WECS. The proposed control approach is practical in power extraction and regulation. Moreover, the drive train's mechanical stresses and output power variations are reduced. In [24], the generator and grid sides converters of a variable-speed WECS are controlled using a second-order sliding mode control method. Results have shown that the proposed control strategy is robust against parametric fluctuation and system uncertainties. Moreover, it minimizes the mechanical load on the wind turbine by preventing chattering in the produced torque. To decrease sub-synchronous control interaction in DFIG-based wind farms, Ref [25] suggested a sliding mode control based on feedback linearization. The findings demonstrate that the proposed technique increases the resilience of the examined system against external disturbances and parameter uncertainty.

The utility grid's stability can be jeopardized if a wind energy plant is abruptly disconnected, especially if this plant is large-scale grid connected. Regulations have been implemented to ensure that the renewable power plant can withstand faults by staying operational even when the voltage drops/rises outside the nominal voltage range for an extended length of time [26]. Moreover, to aid voltage recovery and maintain the system's stability, grid codes require renewable energy power plants to inject reactive currents during faults to the main grid [27]. Depending on the voltage drop or rise, the quantity of absorbed or injected reactive current should be determined [28]. Several methods have been used to fulfill voltage ride-through and reactive current support requirements. These methods either use external devices such as energy storage systems as in [29], [30] or use improved control techniques. In [31], a fuzzy controller is utilized to assist in the case of grid faults via reactive current injection, as required by the standard. In [32], a control strategy has been proposed for a utility-connected PMSG to reduce the transient event oscillations. The stability issue of connecting a large-capacity wind generator to a weak AC grid has been investigated in [33] by providing a stability analysis of a 2-MW variable-speed directly driven generator connected to an ac grid operating under various grid conditions.

In this paper, a sliding mode control scheme is proposed for the converters' control of a grid-connected direct-drive PMSG-based wind turbine. The adopted control law minimizes the chattering effect of the SMC. Furthermore, the LCL filter and its dynamics have been incorporated in the design of the SMC control law to reduce the total harmonic distortion of the grid currents. Finally, since grid codes require the wind energy system to inject reactive current into the grid to aid voltage recovery and maintain the power network's stability, a reactive power control scheme has been introduced to fulfill those requirements. The rest of this paper is organized as follows section II describes the mathematical model and control of the machine-side converter. Section III presents the grid-side converter control, LCL filter design, and reactive power injection scheme. Section IV discusses the simulation results. Section V provides the conclusion of the study.

II. MACHINE-SIDE CONVERTER CONTROL

A. PMSG MODEL

This sub-section gives the mathematical model of the permanent magnet synchronous generator, all the quantities are expressed in per-unit notation. The stator voltages of the PMSG in the d-q frame can be represented as:

$$\begin{bmatrix} v_d \\ v_q \end{bmatrix} = \begin{bmatrix} R_s & -\omega_r L_q \\ \omega_r L_d & R_s \end{bmatrix} \begin{bmatrix} i_{ds} \\ i_{qs} \end{bmatrix} + \begin{bmatrix} L_d/\omega_{base} & 0 \\ 0 & L_q/\omega_{base} \end{bmatrix} \frac{d}{dt} \begin{bmatrix} i_d \\ i_q \end{bmatrix} + \begin{bmatrix} 0 \\ w_r \psi_f \end{bmatrix} \quad (1)$$

where v_d,v_q are the dq-axis stator voltages, i_{ds},i_{qs} are the dq-axis stator currents, L_d, L_q are the dq stator reactances, ψ_f is the peak flux of the PMSG, R_s is the resistance of the stator winding, ω_r represents the electrical speed of the rotor, and ω_{base} is the base electrical speed of the PMSG.

The electromagnetic torque can be obtained using:

$$T_e = \left[\psi_f i_q + \left(L_d - L_q\right) i_d i_q\right] \tag{2}$$

For surface-mount permanent magnet synchronous generator $L_d = L_q = L$, hence (2) can be simplified as:

$$T_e = \psi_f i_q \tag{3}$$

The mechanical dynamics of the PMSG is represented by:

$$2H\frac{d}{dt}\omega_m + B\omega_m = T_e - T_m \tag{4}$$

where H is the inertia time constant, B is the viscous friction, ω_m is the rotor mechanical speed, T_e and T_m denote the electromagnetic and mechanical torque respectively.

B. WIND TURBINE MODEL AND MAXIMUM POWER EXTRACTION STRATEGY

The power output of the wind turbine can be obtained using:

$$P_T = 0.5\pi\rho R^2 v_w^3 C_p(\lambda, \beta) \tag{5}$$

where ρ represents the air density ($kg/m3$), R is the rotor diameter of the wind turbine (m), v_w is the wind speed (m/s), C_p(λ,β) denotes the power coefficient of the rotor blades, which is a function of the tip speed ratio (λ) and the pitch angle (β) and can be calculated in term of the turbine coefficient characteristics constants (C_1 -C_7) as follows.

$$C_p = C_1\left(\frac{C_2}{\lambda_I} - C_3\beta - C_4\beta^2 - C_5\right)e^{-\frac{C_6}{\lambda_I}} + C_7\lambda \tag{6}$$

where the tip speed ratio (λ) and the intermittent tip speed ratio (λ_I) can be obtained by:

$$\lambda = \frac{R\omega_m}{v_w} \tag{7}$$

$$\lambda_I = \left[\frac{1}{\lambda + 0.08\beta} - \frac{0.035}{\beta^3 + 1}\right]^{-1} \tag{8}$$

where ω_m is the mechanical speed of the rotor in (rad/s).

Fig. 2 shows the variation of the wind turbine power coefficient (C_p) versus the tip speed ratio and pitch angle for the wind turbine parameters used in this paper which are shown in the appendix, Table 8. The wind turbine model used in this study has a maximum power coefficient (C_p) of 0.48 obtained at an optimal tip speed ratio (λ) of 8.512 and pitch angle (β) of 0. Then according to (7), the tip speed ratio can be maintained at its optimal value for different wind speeds by adjusting the generator speed in proportion way to the variation of the wind speed. Hence maximum power can be extracted during various wind conditions.

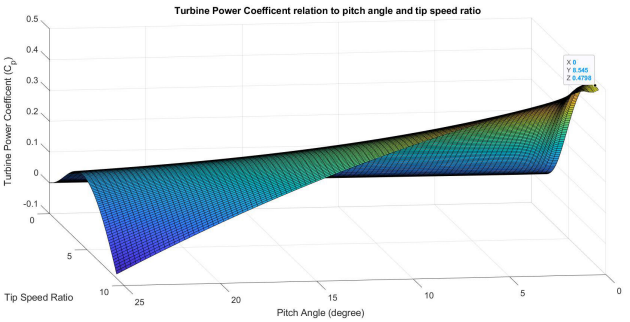

FIGURE 2. Turbine power coefficient's relationship to pitch angle and tip speed ratio.

C. PI CONTROL APPROACH

The control structure of the machine-side converter consists of an outer speed control loop and an inner current control loop. The speed control loop regulates the generator speed to obtain the maximum power extraction, and the output of this loop is the reference electromagnetic torque. The current control loop adjusts the referenced q-axis current to a reference value generated by the speed loop, while the referenced d-axis current is kept at zero to obtain maximum torque per ampere [11].

According to (1), the dq-axis stator currents of the PMSG (i_d, i_q) can be controlled through the dq-axis stator voltages (v_d, v_q). This is achieved by applying a reference dq-axis voltages (v_d*, v_q*) to the converter. The Pulse Width Modulation (PWM) dynamics, digital calculation and time delay are expressed as a first-order system with a time delay (T_s) equals one half of the converter's sampling frequency [34]. Module Optimum (MO), Symmetric Optimum (SO), and zero pole cancellation (ZPC) methods are used to tune the parameters of the speed and current controllers. The detailed procedure of obtaining the controller 's parameters using MO and SO can be found in [17], [35]. The tuning parameter of SO method (σ) has been selected to be in the range of (2-4). For the MSC's current control loop, with ZPC method the zero of the PI controller is selected to cancel the dominant pole of the system,i.e.,setting $K_{ii}/K_{pi} = \omega_b R/L$ and the current controller bandwidth is selected to be 0.1 of the converter's switching frequency [36]–[39].Similarly for the speed control loop setting $K_{is}/K_{ps} = B/2H$. Additionally, the speed controller should act in a slower manner than the inner current controller; hence the bandwidth of the speed controller is selected to be ten times less than the bandwidth of the current controller [39]. Fig. 4 and Table 1 compares the transient response characteristic of the current control loop with different tuning approaches,it can be seen that ZPC has the smallest settling time with minimum overshoot of 0.2%. Similar results are obtained when tuning the MSC's speed control loop as shown in Fig. 5 and Table 2, Although that with SO ($\sigma = 3, 3.5$), the system response is faster, it has a relatively high overshoot. Thus, ZPC parameters are selected taking into consideration that the speed control loop acts

TABLE 1. Performance comparison of various methods used in tuning MSC's current control loop.

Method	Controller Parameters		closed loop step response	
	K_{pi}	K_{ii}	$T_s(ms)$	$M_p(\%)$
MO	10.57	34200	5.1e3	99.5
SO (σ=2.0)	10.57	8560	5.11	43.3
SO (σ=2.5)	8.46	4380	4.95	31.8
SO (σ=3.0)	7.05	2530	7.31	24.8
SO (σ=3.5)	6.04	1590	9.89	20.2
SO (σ=4.0)	5.28	1070	12.6	17.1
ZPC	6.64	10.17	2.54	0.203

TABLE 2. Performance comparison of various methods used in tuning MSC's speed control loop.

Method	Controller Parameters		closed loop step response	
	K_{ps}	K_{is}	$T_s(ms)$	$M_p(\%)$
MO	118.7418	1.2086e+05	226e3	93.9
SO (σ=2.5)	94.9935	1.5471e+04	15.7	32
SO (σ=3.0)	79.1612	8.9529e+03	23.3	24.9
SO (σ=3.5)	67.8525	5.6380e+03	31.5	20.3
SO (σ=4.0)	59.3709	3.7770e+03	40.2	17.3
ZPC	23.7484	0.8200	35.3	-

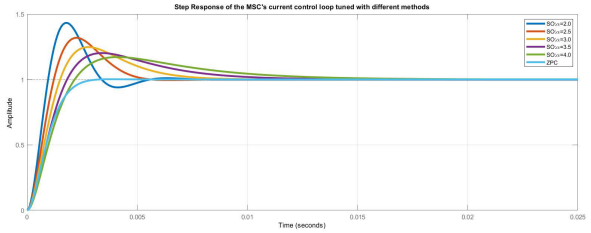

FIGURE 3. Step response of the MSC's current control loop tuned with different methods.

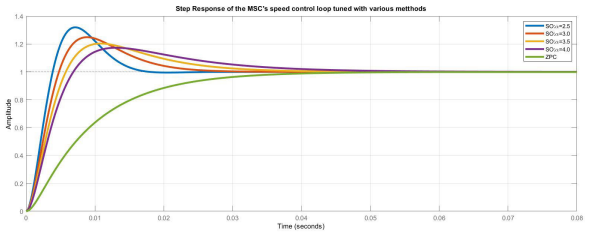

FIGURE 4. Step response of the MSC's speed control loop tuned with different methods.

slower than the current control loop. The block diagram of the machine-side converter's current control is shown in Fig. 5.

D. SMC CONTROL STRATEGY

SMC's control law is set up in such a way that it allows the system to reach equilibrium state. The development of the SMC strategy involves the following procedure:

- Selection of a sliding surface that symbolizes the system's dynamic behavior. The sliding surface is chosen to guarantee that the controlled variable is converging towards its reference value. Typically, a time-varying sliding surface is selected for nth-order system as:

$$s = \left(\frac{d}{dt} + \lambda\right)^{n-1} (x^* - x) \tag{9}$$

where x^* is the reference value of the controlled variable, x is the measured value of the controlled variable, and λ is a positive constant.
- Defining the control law: sliding mode control law is defined by adding together an equivalent control law to a switching control law. The former enables the controlled variable to converge on the sliding surface during the reaching phase, whereas the latter enables the controlled variable to oscillate about the sliding surface during the sliding phase. To maintain the system' dynamic behavior along the sliding surface, sliding mode control law should satisfy the following condition:

$$\dot{s}s \leq 0 \tag{10}$$

An improved reaching law introduced in [40] is adopted in this design to minimize the chattering effect. In order to satisfy the requirements of the preceding expression, $\dot{s}$ is defined as:

$$\dot{s} = -\Lambda s - \frac{\beta}{\mathcal{F}(s)}|s|^{\alpha}\,\text{sign}(s) \tag{11}$$

$$\mathcal{F}(s) = \delta + (1-\delta)e^{-\gamma|s|} \tag{12}$$

where Λ,β,γ are positive numbers, α,δ are between 0 and 1, sign is the sign function.

The simplest reaching law is the constant rate reaching law ($\dot{s} = -\beta\ sign(s)$), in which choosing high value of the gain speed up the system response but also results in a severe chattering. Adding a proportional term ($-\Lambda s$) to the constant rate reaching law forms the exponential reaching law ($\dot{s} = -\beta\ sign(s) - \Lambda s$). the advantage of the additional term is that when s is big, the state is driven to approach the switching surface quicker. The power rate reaching law ($\dot{s} = -\beta\ |s|^{\alpha}\ sign(s)$) has a fast-reaching speed when the state is far away from the switching surface, However, the reaching speed is lowered when the state is close to the switching manifold. The adopted reaching law in (11) combines the merits of the power rate and the exponential reaching law and gives an extra degree of freedom to control the magnitude of chattering as well as the reaching time. In particular having a value of δ between 0 and 1 increases/reduces the reaching time and when $\delta = 1$ the reaching law form will be the same as the power rate law. Moreover, the chattering effect can be minimized by selecting an appropriate value of α.

For the purpose of comparison, the system of equation (13-14) is chosen as an example to compare the existing reaching laws to the adopted one with the objective of maintaining the controlled variable (direct-axis current i_d) at reference value of zero. The derived control laws in (17-18) is implemented with the following parameters ($\Lambda = 30, \beta = 30, \alpha = 0.1/0.9, \delta = 0.1, \gamma = 1$) assuming that the initial value $i_d = 0$. The results are plotted in Fig. 6 which shows that the exponential, constant rate, and power

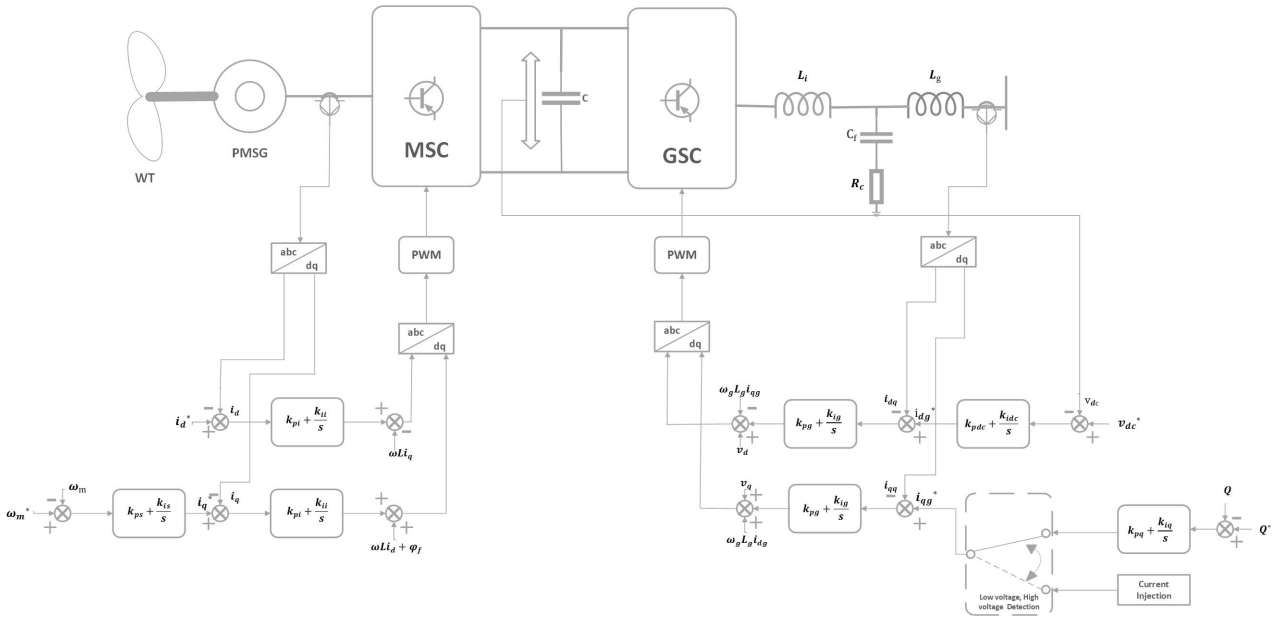

FIGURE 5. PI-based overall control strategy.

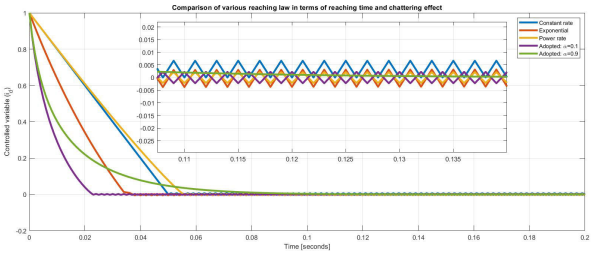

FIGURE 6. Comparison of various reaching laws in term of reaching time and chattering effect.

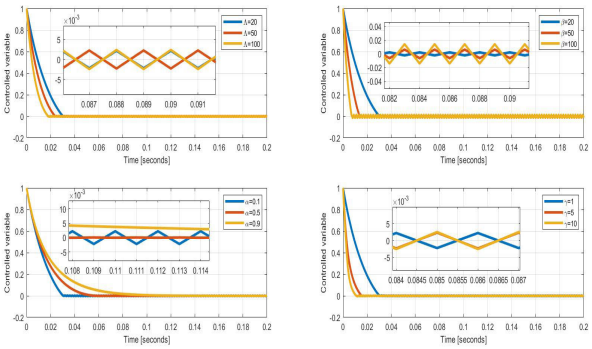

FIGURE 7. The impact of parametric variation of the reaching law.

rate reaching laws have a higher chattering magnitude compared to the adopted reaching law. Moreover, the adjusting of the coefficient α in (10) gives the flexibility to control the chattering amplitude at the expense of the response time. The effect of varying the parameters in (11), (12) is further investigated, Fig. 7 shows how adjusting the value of α can increase/decrease the chattering magnitude. Increasing the value of the gain β speeds up the response considerably but also increases the chattering. The variation in Λ,γ have a relatively small impact on the reaching time with no obvious affect on the chattering. The final tuning values for the SMC's parameters are obtained by trial and error.

Rewriting (1) as:

$$\dot{i_d} = \frac{\omega_{\text{base}}}{L}\left(v_d{}^* - Ri_d + \omega_r L i_q\right) \tag{13}$$

$$\dot{i_q} = \frac{\omega_{\text{base}}}{L}\left(v_q{}^* - Ri_q - \omega_r L i_q - \varphi_f \omega_r\right) \tag{14}$$

Defining the sliding surfaces as:

$$s_d = i_d{}^* - i_d \tag{15}$$

$$s_q = i_q{}^* - i_q \tag{16}$$

The sliding mode on the sliding surfaces satisfy $s_d = \dot{s_d} = s_q = \dot{s_q} = 0$, then using (11), and (13) to (16) the control law for the d-q axis voltages reference can be obtained as:

$$v_d^* = \frac{L}{\omega_{\text{base}}}\dot{i_d}^* + Ri_d - \omega_r L i_q + \frac{L}{\omega_{\text{base}}}\Lambda s_d + \frac{L}{\omega_{\text{base}}}\frac{\beta}{\mathcal{F}(s_d)}|s_d|^{\alpha}\,\text{sign}(s_d) \tag{17}$$

$$v_q{}^* = \frac{L}{\omega_{\text{base}}}\dot{i_q}^* + Ri_q + \omega_r L i_d + \omega_r \varphi_f + \frac{L}{\omega_{\text{base}}}\Lambda s_q + \frac{L}{\omega_{\text{base}}}\frac{\beta}{\mathcal{F}(s_q)}|s_q|^{\alpha}\,\text{sign}(s_q) \tag{18}$$

Equation (4) can be represented as:

$$2H\dot{\omega_m} + B\omega_m = \varphi_f i_q - T_m \tag{19}$$

The sliding surface is then defined as:

$$s_w = \omega_m^* - \omega_m \tag{20}$$

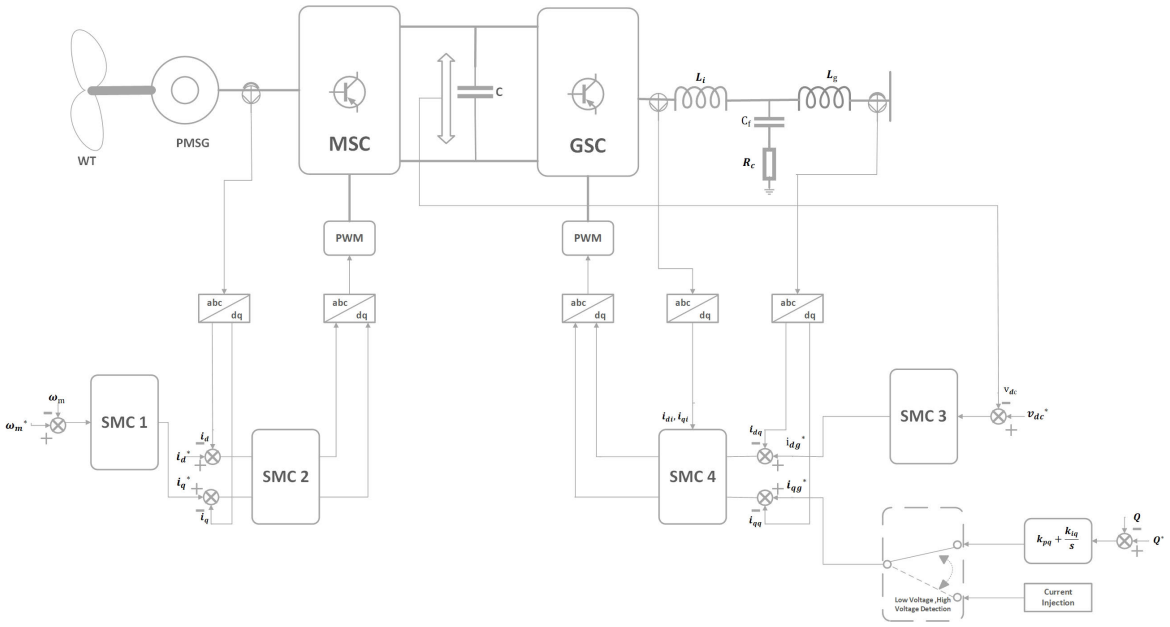

FIGURE 8. SMC-based overall control strategy.

Since the sliding mode on the sliding surfaces satisfy $\dot{s_w} = 0$, using (11), and (19) the following expression of the referenced q-axis current can be obtained:

$$i_q{}^* = \frac{2H}{\varphi_f}\dot{\omega}_m{}^* + \frac{T_m}{\varphi_f} + \frac{B}{\varphi_f}\omega_m + \frac{2H}{\varphi_f}\Lambda s_w + \frac{2H}{\varphi_f}\frac{\beta}{\mathcal{F}(s_w)}|s_w|^{\alpha}\,\text{sign}(s_w) \quad (21)$$

The referenced value of the direct-axis current ($i_d{}^*$) is set at zero, hence ($\dot{i_d}{}^*$) in (17) is assumed to be zero. The referenced value of the quadrature-axis current ($i_q{}^*$) in (18) is obtained by the speed control loop and it assumed that its derivable. The optimal speed ($\omega_m{}^*$) in (20) is calculated based on the optimal tip speed ratio and its derivative in (21) is assumed to be known. The block diagram of the SMC control strategy is shown in Fig. 8.

E. STABILITY ANALYSIS

Lyapunov stability theory is used for the stability analysis of SMC control low, Defining the following Lyapunov function:

$$\sigma_1 = \frac{1}{2}s_d^2 + \frac{1}{2}s_q^2 + \frac{1}{2}s_w^2 \quad (22)$$

Then:

$$\dot{\sigma_1} = s_d\dot{s_d} + s_q\dot{s_q} + s_w\dot{s_w} \quad (23)$$

Differentiating (15), (16), and (20) then substituting in (23):

$$\dot{\sigma_1} = s_d\left(\dot{i_d}{}^* - \frac{\omega_{\text{base}}}{L}\left(v_d{}^* - Ri_d + \omega_r L i_q\right)\right) + s_q\left(\dot{i_q}{}^* - \frac{\omega_{\text{base}}}{L}\left(v_q{}^* - Ri_q - \omega_r L i_q - \varphi_f\omega_r\right)\right) + s_w\left(\dot{\omega_m}{}^* - \frac{1}{2H}\left(\varphi_f i_q - T_m - B\omega_m\right)\right) \quad (24)$$

Substituting the control laws in (17), (18), and (21):

$$\dot{\sigma_1} = s_d\left(-\Lambda s_d - \frac{\beta}{\mathcal{F}(s_d)}|s_d|^{\alpha}\,\text{sign}(s_d)\right) + s_q\left(-\Lambda s_q - \frac{\beta}{\mathcal{F}(s_q)}|s_q|^{\alpha}\,\text{sign}(s_q)\right) + s_w\left(-\Lambda s_w - \frac{\beta}{\mathcal{F}(s_w)}|s_w|^{\alpha}\,\text{sign}(s_w)\right) \quad (25)$$

Hence the asymptotical stability is guaranteed with the following condition satisfied:

$$\dot{\sigma_1} = -\Lambda s_d s_d - \frac{\beta}{\mathcal{F}(s_d)}s_d|s_d|^{\alpha}\,\text{sign}(s_d) - \Lambda s_q s_q - \frac{\beta}{\mathcal{F}(s_q)}s_q|s_q|^{\alpha}\,\text{sign}(s_q) - \Lambda s_w s_w - \frac{\beta}{\mathcal{F}(s_w)}s_w|s_w|^{\alpha}\,\text{sign}(s_w) < 0 \quad (26)$$

III. GRID-SIDE CONVERTER CONTROL

A. GSC AND DC LINK MODEL

The grid connection of the machine-side converter can be modeled in the dq-frame as:

$$\begin{bmatrix} v_{di} \\ v_{qi} \end{bmatrix} = \begin{bmatrix} R_g & -\omega_g L_g \\ \omega_g L_g & R_g \end{bmatrix}\begin{bmatrix} i_{dg} \\ i_{qg} \end{bmatrix} + \begin{bmatrix} L_g/\omega_{g,b\,ase} & 0 \\ 0 & L_g/\omega_{g,b\,ase} \end{bmatrix}\frac{d}{dt}\begin{bmatrix} i_{dg} \\ i_{qg} \end{bmatrix} + \begin{bmatrix} v_{dg} \\ v_{qg} \end{bmatrix} \quad (27)$$

where v_{di}, v_{qi} are the d-q components of the converter voltage, v_{dg},v_{dg} are the d-q axis grid voltage at the point of common coupling. R_g,L_g are the grid resistance and inductance respectively. i_{dg},i_{qg} are the d-q components of the grid current and ω_g denotes the grid frequency. The grid active and reactive power can be obtained as follows:

$$P_g = v_{dg}i_{dg} + v_{qg}i_{qg} \tag{28}$$

$$Q_g = v_{qg}i_{dg} - v_{dg}i_{qg} \tag{29}$$

And the DC link dynamics can be expressed as:

$$c\frac{dv_{dc}}{dt} = \left(\frac{v_{dg}i_{dg}}{v_{dc}} + \frac{v_{qg}i_{qg}}{v_{dc}}\right) - i_{dc} \tag{30}$$

where c is the DC link capacitance, v_{dc},i_{dc} are the DC link voltage and current, respectively.

By aligning the d-axis components of the grid voltage with the grid voltage vector, the q-axis becomes zero which facilitate the control design and equations (28) to (30) can be simplified further to:

$$P_g = v_{dg}i_{dg} \tag{31}$$

$$Q_g = -v_{dg}i_{qg} \tag{32}$$

$$c\frac{dv_{dc}}{dt} = \left(\frac{v_{dg}i_{dg}}{v_{dc}}\right) - i_{dc} \tag{33}$$

B. PI CONTROL APPROACH

The relations defined in (32), and (33) indicate that the reactive power and DC link voltage can be controlled by the q-axis and d-axis grid current, respectively. Thus, the control structure of the GSC converter consists of two control loops, a current control loop that regulates the d-q axis grid currents (i_{dg}, i_{qg}) and a DC link voltage control loop that adjusts the DC link voltage at its reference value and generate the referenced d-axis current loop.

The grid-side converter current loop can be derived using (27) in a similar manner to the machine-side converter current loop, and the PI controller acts to eliminate the error between the dq-axis grid currents and their referenced values. PWM dynamics are expressed as a first-order system. Similar to the design procedure followed in tuning MSC current loop controller with ZPC i.e., setting $K_{ig}/K_{pg} = \omega_{gbase}R_g/L_g$. With $K_{pg} = f_{sw}L_g/(3\omega_{gbase})$ [41]. f_{sw} represents the switching frequency of the grid-side converter. The results of using different methods to adjust the GSC' current controller gains are shown in Table 3 and Fig. 9 The findings are very close to those of the MSC current loop, MO method produces a slow oscillatory response, SO method gives a fast response but high overshoot. ZPC gives an acceptable overshoot without sacrificing the response speed.

In the design of the DC link voltage controller, the closed loop transfer function of the GSC current loop is expressed as a first-order system with a time constant (T_c). After linearization of (33) around the converter operating point, the block diagram of the DC link voltage loop can be obtained. Symmetric optimum is used to design DC link voltage controller. Fig. 10 shows the dynamic characteristic of the closed loop response for different values of the tuning parameter. The value of ($\sigma = 4$) is chosen as it results in an overshoot less than 20% and acceptable settling time of (57.8 ms) as shown in Table 4.

TABLE 3. Performance comparison of various methods used in tuning GSC's speed control loop.

Method	Controller Parameters		closed loop step response	
	K_{pg}	K_{ig}	$T_s(ms)$	$M_p(\%)$
MO	1.4291	7.7172e+03	0.413e3	99.2
SO (σ= 2.0)	1.4291	1.9293e+03	3.05	42.6
SO (σ=2.5)	1.1433	987.8019	2.98	31.1
SO (σ=3.0)	0.9527	571.6446	4.4	23.9
SO (σ=3.5)	0.8166	359.9861	5.94	19.2
SO (σ=4)	0.7146	241.1626	7.54	16.1
ZPC	0.5308	2.5207	6.65	-

TABLE 4. Performance comparison of various methods used in tuning GSC's DC voltage loop.

Method	Controller Parameters		closed loop step response	
	K_{pdc}	K_{idc}	$T_s(ms)$	$M_p(\%)$
SO (σ=2.0)	2.8657	386.8645	30.6	43.3
SO (σ=2.5)	2.2925	198.0746	29.7	32
SO (σ=3.0)	1.9104	114.6265	45.3	22.8
SO (σ=3.5)	1.6375	72.1846	59.4	20.3
SO (σ=4.0)	1.4328	48.3581	57.8	17.3

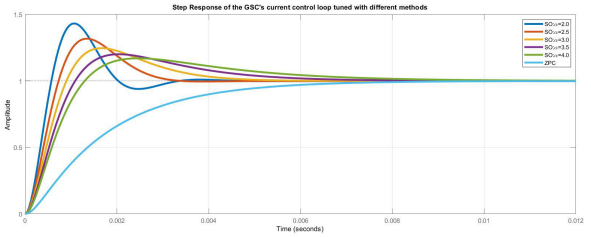

FIGURE 9. Step response of the GSC's current control loop tuned with different methods.

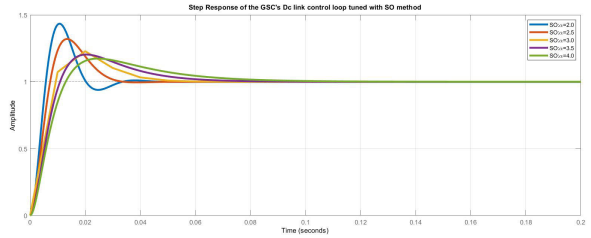

FIGURE 10. Step response of the GSC's DC voltage control loop tuned with different methods.

C. SMC CONTROL STRATEGY FOR GSC's CURRENT CONTROL

The grid connection of the machine-side converter can be modeled in the dq-frame as:

$$\dot{i_{dg}} = \frac{\omega_{g\,\text{base}}}{L_g}\left(v_{di} - R_g i_{dg} + \omega_g L_g i_{qg} - v_{dg}\right) \tag{34}$$

$$\dot{i_{qg}} = \frac{\omega_{g\,\text{base}}}{L_g}\left(v_{qi} - R_g i_{qg} - \omega_g L_g i_{dg} - v_{qg}\right) \tag{35}$$

Defining the sliding surfaces as:

$$s_{dg} = {i_{dg}}^* - i_{dg} \tag{36}$$

$$s_{qg} = {i_{qg}}^* - i_{qg} \tag{37}$$

Similarly, using (11), and (34) to (37) the following control law for the referenced d-q axis voltages can be obtained.

$$\begin{aligned} {v_{di}}^* = & \frac{L_g}{\omega_{g,\text{ base}}} \dot{{i_{dg}}^*} + R_g i_{dg} - \omega_g L_g i_{qg} + v_{dg} \\ & + \frac{L_g}{\omega g_{\text{base}}} \Lambda s_{dg} + \frac{L_g}{\omega g_{\text{base}}} \frac{\beta}{\mathcal{F}\left(s_{dg}\right)} \left|s_{dg}\right|^{\alpha} \text{sign}\left(s_{dg}\right) \end{aligned} \tag{38}$$

$$\begin{aligned} {v_{qi}}^* = & \frac{L_g}{\omega_{g,\text{ base}}} \dot{{i_{qg}}^*} + R_g i_{qg} + \omega_g L_g i_{dg} + v_{qg} \\ & + \frac{L_g}{\omega g_{\text{base}}} \Lambda s_{qg} + \frac{L_g}{\omega g_{\text{base}}} \frac{\beta}{\mathcal{F}\left(s_{qg}\right)} \left|s_{qg}\right|^{\alpha} \text{sign}\left(s_{qg}\right) \end{aligned} \tag{39}$$

The referenced values of $({i_{dg}}^*)$, $({i_{qg}}^*)$ are determined by the DC link control loop and the reactive power injection scheme, respectively and their derivatives in (38)-(39) is assumed to be known.

D. LCL FILTER DESIGN

The procedure given in [41] is adopted. Due to the neglection of the capacitor branch in the PI control design, the LCL filter acts roughly like an equivalent L-filter in the low frequency domain [42]. As a results, the same procedure used to tune the PI controller while using a L filter may be used to tune the controller when using an LCL filter [41]. The consideration of LCL filter in the design of the SMC control laws is described as follows:

The mathematical model of the LCL filter in the dq- reference frame can be given by:

$$\begin{aligned} \dot{i_{di}} = & \frac{\omega_{gbase}}{L_i} [v_{di} - v_{cd} - (R_i + R_c)\, i_{di} \\ & + \omega_g L_i i_{qi} + R_c i_{dg}] \end{aligned} \tag{40}$$

$$\begin{aligned} \dot{i_{qi}} = & \frac{\omega_{gbase}}{L_i} [v_{qi} - v_{cq} - (R_i + R_c)\, i_{qi} \\ & - \omega_g L_i i_{di} + R_c i_{qg}] \end{aligned} \tag{41}$$

$$\begin{aligned} \dot{i_{dg}} = & \frac{\omega_{gbase}}{L_i} [v_{cd} - v_{dg} - \left(R_g + R_c\right) i_{dg} \\ & + \omega_g L_g i_{qg} + R_c i_{di}] \end{aligned} \tag{42}$$

$$\begin{aligned} \dot{i_{qg}} = & \frac{\omega_{gbase}}{L_i} [v_{cq} - v_{qg} - \left(R_g + R_c\right) i_{qg} \\ & - \omega_g L_g i_{dg} + R_c i_{qi}] \end{aligned} \tag{43}$$

$$i_{di} = i_{cd} + i_{dg} \tag{44}$$

$$i_{qi} = i_{cq} + i_{qg} \tag{45}$$

where i_{di},i_{qi} are the d-axis and q-axis components of the GSC 'output current, v_{di},v_{qi} are the d-axis and q-axis components of the GSC 'output voltage, i_{dg},i_{qg} are the d-axis and q-axis components of the injected current to the grid, v_{dg},v_{qg} are the d-axis and q-axis components of the grid voltage, i_{cd},i_{cq} are the d-axis and q-axis components of the capacitor current. v_{cd},v_{cq} are the d-axis and q-axis components of the capacitor voltages, respectively. R_i,L_i are the converter-side resistance and inductance, respectively. R_g,L_g are the grid-side resistance and inductance, respectively, R_c is the damping resistance.

Similar to the procedure given in section III.C, the referenced d-q axis voltages can be obtained in this case as:

$$\begin{aligned} {v_{di}}^* = & \frac{L_g}{\omega_{g,b\ ase}} \dot{idg^*} + \frac{L_i}{\omega_{g,b\ ase}} \dot{i_{di}} + R_g i_{dg} \\ & - \omega_g L_g i_{qg} + v_{dg} + R_i i_{di} - L_i w_g i_{qi} + \frac{L_g}{\omega g_{base}} \Lambda s_{dg} \\ & + \frac{L_g}{\omega g_{base}} \frac{\beta}{\mathcal{F}\left(s_{dg}\right)} \left|s_{dg}\right|^{\alpha} \text{sign}\left(s_{dg}\right) \end{aligned} \tag{46}$$

$$\begin{aligned} {v_{qi}}^* = & \frac{L_g}{\omega_{g,b\ ase}} \dot{iqg^*} + \frac{L_i}{\omega_{g,b\ ase}} \dot{i_{qi}} + R_g i_{qg} \\ & + \omega_g L_g i_{dg} + v_{qg} + R_i i_{qi} + L_i w_g i_{di} + \frac{L_g}{\omega g_{base}} \Lambda s_{qg} \\ & + \frac{L_g}{\omega g_{base}} \frac{\beta}{\mathcal{F}\left(s_{qg}\right)} \left|s_{qg}\right|^{\alpha} \text{sign}\left(s_{qg}\right) \end{aligned} \tag{47}$$

E. SMC STRATEGY FOR THE DC-LINK VOLTAGE REGULATION

The DC-link dynamic can be described by:

$$P_s - v_{dg} i_{dg} = \frac{c}{\omega g_{base}} v_{dc} \dot{v_{dc}} \tag{48}$$

Defining the sliding surface as:

$$s_{dc} = {v_{dc}}^* - v_{dc} \tag{49}$$

Since the sliding mode on the sliding surface satisfies $\dot{s_{dc}} = 0$,Utilizing (11), (48), and (49) the following control law can be obtained:

$$\begin{aligned} i_{dg}^* = & v_{dg} P_s - \frac{v_{dc}}{v_{dg}} \frac{C}{\omega g_{base}} \dot{{v_{dc}}^*} - \frac{v_{dc}}{v_{dg}} \frac{C}{\omega g_{base}} \Lambda s_{dc} \\ & - \frac{v_{dc}}{v_{dg}} \frac{C}{\omega g_{base}} \frac{\beta}{\mathcal{F}\left(s_{dc}\right)} \left|s_{dc}\right|^{\alpha} \text{sign}\left(s_{dc}\right) \end{aligned} \tag{50}$$

The DC link referenced voltage $({v_{dc}}^*)$ is set at 1220 v, hence the value of $(\dot{{v_{dc}}^*})$ in (50) is considered zero.

F. STABILITY ANALYSIS

Defining the following Lyapunov function:

$$\sigma_2 = \frac{1}{2} s_{dg}^2 + \frac{1}{2} s_{qg}^2 + \frac{1}{2} s_{dc}^2 \tag{51}$$

Then differentiating (51):

$$\dot{\sigma}_2 = s_{dg} \dot{s}_{dg} + s_{qg} \dot{s}_{qg} + s_{dc} \dot{s}_{dc} \tag{52}$$

Differentiating (36), (37), and (49). Then substituting in (52) with the help of (40) to (43), and (48):

$$\begin{aligned} \dot{\sigma}_2 = & s_{dc} \left({v_{dc}}^* - \frac{\omega g_{base}}{c v_{dc}} \left(P_s - v_{dg} {i_{dg}}^*\right) \right) \\ & + s_{dg} \left({i_{dg}}^* - \frac{\omega_{gbase}}{L_g} \left({v_{di}}^* - R_g i_{dg} + \omega_g L_g i_{qg} - v_{dg}\right) \right) \end{aligned}$$

$$+s_{qg}\left(i_{qg}{}^{*}-\frac{\omega_{gbase}}{L_g}\left(v_{qi}{}^{*}-\ R_g i_{qg}-\omega_g L_g i_{dg}-v_{qg}\right)\right) \tag{53}$$

Substituting the control laws (46), (47), and (50) in (53):

$$\begin{aligned}\dot{\sigma}_2 = {} & s_{dg}\left(-\Lambda s_{dg}-\frac{\beta}{\mathcal{F}\left(s_{dg}\right)}\left|s_{dg}\right|^{\alpha}\operatorname{sign}\left(s_{dg}\right)\right)\\ & +s_{qg}\left(-\Lambda s_{qg}-\frac{\beta}{\mathcal{F}\left(s_{qg}\right)}\left|s_{qg}\right|^{\alpha}\operatorname{sign}\left(s_{qg}\right)\right)\\ & +s_{dc}\left(-\Lambda s_{dc}-\frac{\beta}{\mathcal{F}\left(s_{dc}\right)}\left|s_{dc}\right|^{\alpha}\operatorname{sign}\left(s_{dc}\right)\right)\end{aligned} \tag{54}$$

Hence the asymptotical stability is guaranteed with the following condition satisfied:

$$\begin{aligned}\dot{\sigma}_2 = {} & -\Lambda s_{dg}s_{dg}-\frac{\beta}{\mathcal{F}\left(s_{dg}\right)}s_{dg}\left|s_{dg}\right|^{\alpha}\operatorname{sign}\left(s_{dg}\right)\\ & -\Lambda s_{qg}s_{qg}-\frac{\beta}{\mathcal{F}\left(s_{qg}\right)}s_{qg}\left|s_{qg}\right|^{\alpha}\operatorname{sign}\left(s_{qg}\right)-\Lambda s_{dc}s_{dc}\\ & -\frac{\beta}{\mathcal{F}\left(s_{dc}\right)}s_{dc}\left|s_w\right|^{\alpha}\operatorname{sign}\left(s_w\right)<0\end{aligned} \tag{55}$$

G. REACTIVE POWER INJECTION

In case of the terminal voltage of the PMSG is below 0.9 *pu* or above 1.1 *pu*, the reactive power control scheme is shifted from a unity power factor operation ($Q^{*}=0$) to actively supply reactive power current to the grid. The amount of the reactive power current ($i_{qg}{}^{*}$) injected to the grid is determined by:

$$i_{qg}{}^{*}=\left\{\begin{array}{ll}2(1-v)\cdot I_N & v>1.1\ pu\\ 1.5(1-v).I_N & 0.9>v\geq 0.2\ pu\\ 1.78.I_N & v<0.2\ pu\end{array}\right\} \tag{56}$$

where v_N, I_N are the nominal voltage and current, respectively.

IV. RESULTS AND DISCUSSION

To validate the effectiveness of the proposed control method, the system of Fig. 11 is modeled and simulated on MATLAB/Simulink. Both configurations of the PI and SMC control strategies (Fig. 5 and Fig. 8) have been implemented. The detailed parameters of the wind turbine, the PMSG, transmission line, and the control parameters are listed in the appendix. A time-domain simulation is used with a discrete step of 50 μs. The generator-side converter and grid-side converter are modeled with the average-model-based block in Simulink with a switching frequency of 1620 and 2700 Hz, respectively. The grid voltage phase and frequency are obtained using PLL. The results are divided in four sections, the first discusses the overall performance of the control strategies in case of a step change in the wind speed, the second compares the total harmonic distortion of the control methods with the consideration of RL and LCL filter, the third presents the proposed system's performance during low voltage and high voltage grid disturbances, the fourth shows the behavior of the system with model uncertainties and measurements noise.

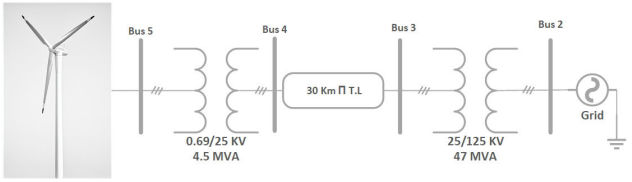

FIGURE 11. Simulated system.

A. STEP CHANGE IN WIND SPEED

With the wind speed profile depicted in Fig. 12, the resulting injected power to the grid varies. The generated active power reaches a steady-state in about 1.2 s. The instantaneous rise/drop in the wind speed at time 5s, 10s, and 15s results in a transient fluctuation in the DC link voltage and this reflects on the generated active power, causing a slight dip as shown in Fig. 13.

During various wind speed conditions, the DC link voltage is maintained at its pre-set value at 1220 V, as it can be seen in Fig. 14. The proposed control method has less magnitude fluctuations compared to the conventional PI method during transients. Fig. 15 depicts the rotor mechanical speed of the PMSG. The speed controller regulates the rotating speed of the PMSG in response to changes in the wind to maintain the ideal tip speed ratio. Both control methods have achieved good reference tracking capability. However, with the PI control, there is a slight mismatch between the reference and actual speed. Fig. 16 shows the three-phase grid currents at

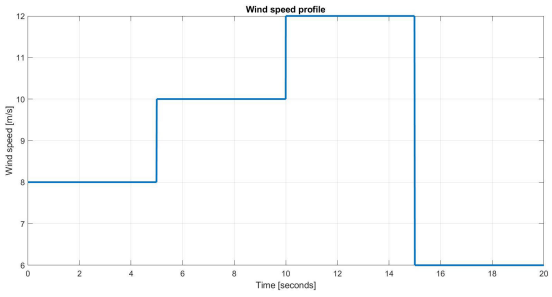

FIGURE 12. Wind speed profile.

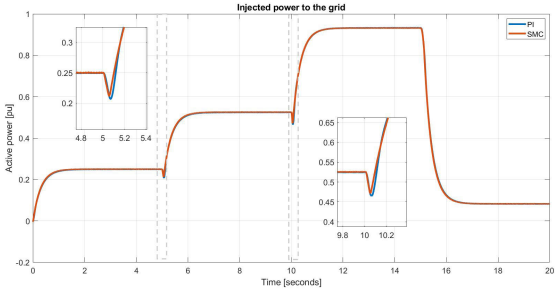

FIGURE 13. Generated active power.

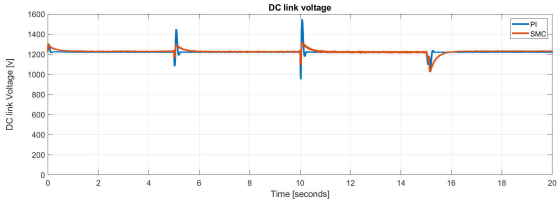

FIGURE 14. DC-link voltage.

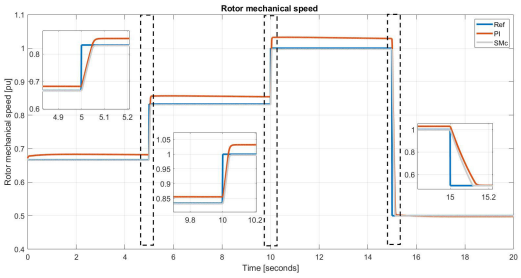

FIGURE 15. PMSG mechanical speed.

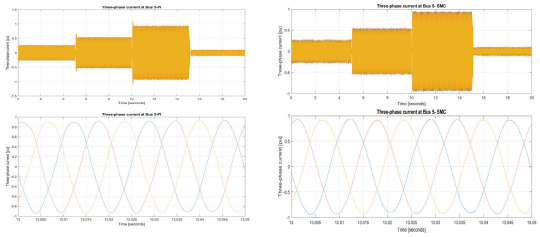

FIGURE 16. (From left-to-right top-to-bottom) Three-phase current at Bus 5-PI,Three-phase current at Bus 5-SMC, Three-phase current at Bus 5-PI (magnified), Three-phase current at Bus 5-SMC (magnified).

Bus 5, the quantity of grid currents is directly proportional to the wind speed variation.

B. THD ANALYSIS

To determine the THD of the grid currents, a 5s simulation of the system in Fig. 11 has been made; considering the PMSG operating at full-rated condition, the steady-state total harmonic distortion results are shown in Table 5. Using the LCL filter instead of the RL filter, with the same total inductance, has significantly reduced the THD. Moreover, two factors have contributed to having the proposed SMC control method less THD than the conventional PI approach. First, the consideration of the LCL filter dynamics in the sliding mode control law design and, second, the SMC reaching law adopted in (11). Fig. 17 shows the current THD at bus 3 of both control methods.

C. LOW-VOLTAGE AND HIGH-VOLTAGE RIDE THROUGH CAPABILITY

Wind energy systems are not only obliged to remain connected but are also required to inject reactive current into the grid during grid voltage disturbances. The low voltage ride-through performance of the proposed system has been validated with the voltage disturbances events described in Table 6. All the events are occurred at time t = 2.5s.

TABLE 5. THD results.

	RL Filter		LCL Filter	
	PI	SMC	PI	SMC
Voltage (Bus 5)	7.79 %	10.88 %	1.00 %	0.94 %
Current (Bus 5)	3.57 %	3.65 %	2.31 %	1.88 %
Current (Bus 4)	3.58 %	3.66 %	2.32 %	1.88 %
Current (Bus 3)	6.89 %	6.11 %	2.39 %	1.97 %
Current (Bus 2)	7.09 %	6.30 %	2.47 %	2.03 %

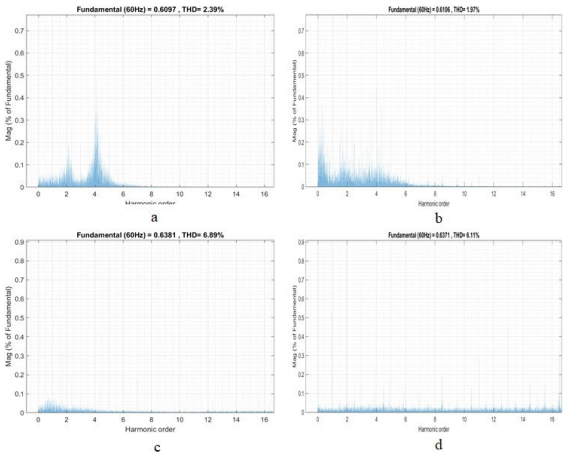

FIGURE 17. THD of the current at Bus 3. (a) PI- with RL filter. (b) SMC-with RL filter. (c) PI-with LCL filter. (d) SMC-with LCL filter.

TABLE 6. low voltage and high voltage cases.

	Voltage percent	Duration (ms)
Case 1	00%	150
Case 2	30%	600
Case 3	80%	1250
Case 4	120%	1250

Fig. 18 shows the three-phase voltage, active and reactive power injected to the grid, and the DC link voltage when 100% three-phase voltage dip is applied to the system, it can be seen that the voltage at the turbine bus is higher than 0 pu because of the voltage support and reactive current injection. During the grid voltage's disturbance, the wind turbine continues to deliver active power, resulting in a mismatch between the active power generated and the active power delivered to the grid, which subsequently causes the DC-link voltage to rise rapidly as a result of the imbalance. However, the transient performance of DC-link voltage of the sliding mode control during the disturbance is smoother than those of the PI. Fig. 19 depicts the system performance when a 70% voltage dip took place; during the fault, the DC-link voltage with PI control reaches a level above 1600 V causes the activation of the crowbar protection (switches on at 1600 V and switches off at 1350 V). Whereas with the SMC control, the DC link voltage is maintained below 1600. The generated active power waveform is smoother and has less fluctuations compared to the PI. It is also noticeable that, when a slight disturbance occurs, i.e., in the case of a 20% voltage dip shown in Fig. 20, the transient performance of the DC voltage, active, and reactive power of both control schemes are close. However, when a significant disturbance occurs, the SMC's

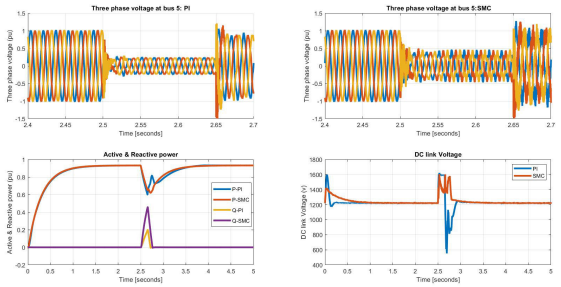

FIGURE 18. Case 1: 100% voltage dip: (From left-to-right then top-to-bottom) Three-phase voltage at Bus 5-PI,Three-phase voltage at Bus 5-SMC, Active and reactive power, DC link voltage.

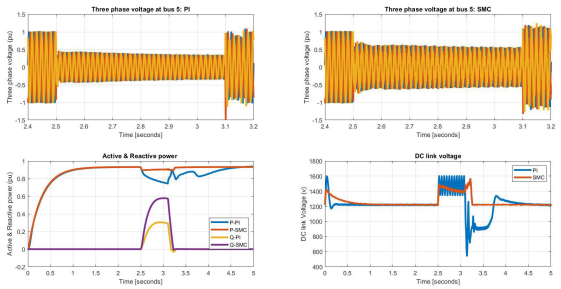

FIGURE 19. Case 2: 70% voltage dip: (From left-to-right then top-to-bottom) Three-phase voltage at Bus 5-PI,Three-phase voltage at Bus 5-SMC, Active and reactive power, DC link voltage.

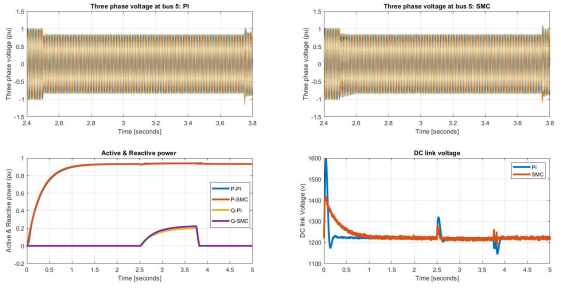

FIGURE 20. Case 3: 20% voltage dip: (From left-to-right then top-to-bottom) Three-phase voltage at Bus 5-PI,Three-phase voltage at Bus 5-SMC, Active and reactive power, DC link voltage.

dynamic performance outperforms those of the PI. This is due to the fact that the linear control design depends on the linearization around specific operation points and the PI controller performance deteriorates when the system operates far from those operational points. Fig. 21 depicts the system performance when the grid voltage reaches 1.2 pu, in this case reactive power is absorbed from the grid.

The wind turbine remained connected to the grid, and the power system's stability was maintained by regulating active and reactive power production, according to the findings. The amount of voltage drop/rise in a fault condition causes a reduction in active power generation. To compensate for the lower/higher voltage, reactive power output rises/falls. When the fault is cleared, active and reactive power generation returns to normal with a reasonable amount of time.

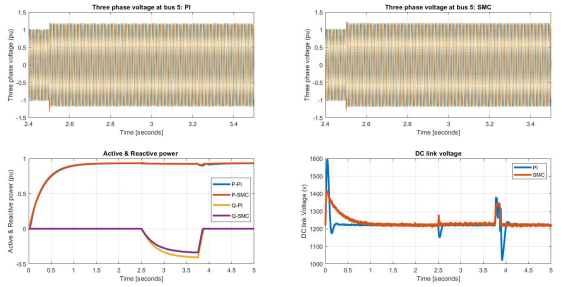

FIGURE 21. Case 4: 120% voltage swell: (From left-to-right then top-to-bottom) Three-phase voltage at Bus 5-PI,Three-phase voltage at Bus 5-SMC, Active and reactive power, DC link voltage.

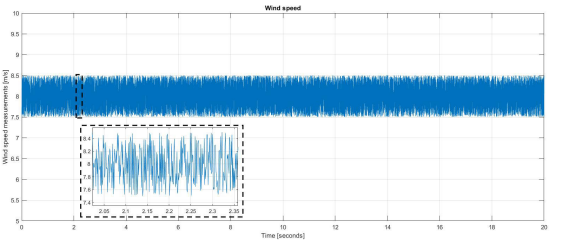

FIGURE 22. wind speed measurements with noise.

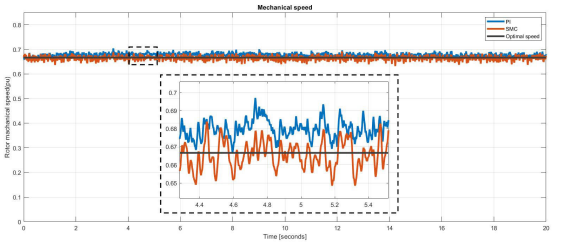

FIGURE 23. Model uncertainty with noise case: Rotor's mechanical speed.

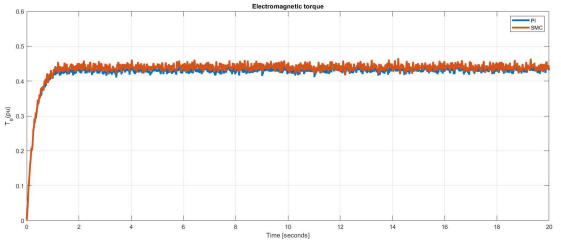

FIGURE 24. Model uncertainty with noise case:Electromagnetic torque.

D. IMPACT OF PARAMETERS CHANGE AND MODEL UNCERTAINTY

Parameter uncertainty and noise are introduced in the system to further investigate the performance of the suggested system. For the electrical system, the stator inductance is reduced by 10% and the stator resistance is raised by 20%. The moment of inertia and viscous friction coefficients of the mechanical system are increased by 20%. Furthermore, the wind speed measurements is exposed to random noise in the range of ± 0.5 m/s. Assuming an initial speed of 0.67 *pu* the impact of parameter's variation and model uncertainty on the rotor mechanical speed, electromagnetic torque and DC link voltage are shown Fig. 22 to Fig. 25. It can

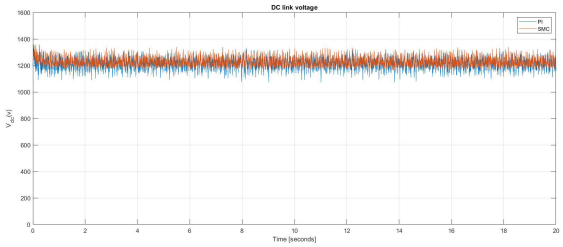

FIGURE 25. Model uncertainty with noise case:DC link voltage.

be observed that the proposed system has maintained the rotor's speed around its optimal value. There is no significant impact on the response time as it can be seen in Fig. 24. However, the DC link voltage fluctuations are higher with the noise measurements introduced to the system.

V. CONCLUSION

This paper proposes a sliding mode control strategy for the converters of a grid-connected direct-drive PMSG-based wind turbine. The performance of the proposed control method has been compared with the conventional PI control taking into consideration the THD as well as the dynamic performance during low/high voltage conditions. With the RL filter, the current total harmonic distortion results of the SMC method at the point of common coupling (Bus 4) is 2% higher than those of the PI control. However, with the inclusion of the LCL filter, the SMC achieved 18% less current THD compared to the PI control. Furthermore, the DC-link voltage and the injected active power into the grid are less disrupted during grid disturbances; hence the proposed control method achieves smooth and stable integration of wind power into the grid.

TABLE 7. RL and LCL filter parameters.

Parameter	RL Filter	LCL Filter
Converter-side inductance	0.1560 mH	0.0780 mH
Converter-side inductance	0.7408 $m\Omega$	0.3704 $m\Omega$
Filter capacitor		6170 μF
Damping Resistor		0.0450 Ω
Grid-side inductance		0.0780 mH
Grid-side resistance		0.3704 mH

TABLE 8. Wind turbine and PMSG parameters.

Wind Turbine		PMSG	
Parameter	Value	Parameter	Value
Rated Power	3 MW	Rated power	3 MW
Rated speed	22.5 rpm	Rated mechanical speed	2.36 (rad/s)
Rotor Radius	43.36 m	Stator Resistance	1.63 $(m\Omega)$
Rated wind speed	12 m/s	Stator Leakage Inductance	0.96(mH)
Cut-in speed	3 m/s	Flux linkage	8.53 (Wb)
Cut-off speed	25 m/s	Shaft moment of inertia	117000 $(kg.m^2)$
Turbine Constant	0.3915	Viscous friction	4040 $(N.m.s)$
Turbine Constant	116	Pole pair	26
Turbine Constant	0.4		
Turbine Constant	0		
Turbine Constant	5		
Turbine Constant	21		
Turbine Constant	0.0192		

APPENDIX

See Tables 7–11.

TABLE 9. Transmission line parameters.

Parameter	Value	Parameter	value
Positive-sequence resistance	0.1153 Ω/km	Positive-sequence inductance	11.33 nF/km
Zero-sequence resistance	0.413 Ω/km	Zero-sequence inductance	5.01 nF/km
Positive-sequence capacitance	1.05 mH/km	Line length	30 km
Zero-sequence capacitance	3.32 mH/km		

TABLE 10. Control design parameters.

Control loop	PI	SMC
MSC- current control	k_{pi} = 6.65 k_{ii} = 10.18	α = 0.1 γ = 2 δ = 0.025 β = 185 Λ = 150
GSC- current control	k_{pg} = 0.53 k_{ig} = 2.52	α = 0.9 γ = 5 δ = 0.025 β = 90 Λ = 50
Speed control	k_{ps} = 23.75 k_{is} = 0.82	α = 0.9 γ = 5 δ = 0.025 β = 75 Λ = 80
DC link	k_{pdc} = 1.43 k_{idc} = 48.36	α= 0.9 γ = 4 δ = 0.9 β = 160 Λ = 240
Reactive power control	k_{pq} = 200 k_{iq} = 1200	

REFERENCES

[1] K.-C. Tseng and C.-C. Huang, "High step-up high-efficiency interleaved converter with voltage multiplier module for renewable energy system," *IEEE Trans. Power Electron.*, vol. 61, no. 3, pp. 1311–1319, Mar. 2014.
[2] H. Armghan, M. Yang, A. Armghan, and N. Ali, "Double integral action based sliding mode controller design for the back-to-back converters in grid-connected hybrid wind-PV system," *Int. J. Electr. Power Energy Syst.*, vol. 127, May 2021, Art. no. 106655.
[3] V. Khare, S. Nema, and P. Baredar, "Solar–wind hybrid renewable energy system: A review," *Renew. Sustain. Energy Rev.*, vol. 58, pp. 23–33, May 2016.
[4] A. Rajaei, M. Mohamadian, and A. Y. Varjani, "Vienna-rectifier-based direct torque control of PMSG for wind energy application," *IEEE Trans. Ind. Electron.*, vol. 60, no. 7, pp. 2919–2929, Jul. 2013.
[5] *Renewable capacity statistics 2020 International Renewable Energy Agency*, IRENA, Abu Dhabi, United Arab Emirates, 2020.
[6] M. E. Haque, M. Negnevitsky, and K. M. Muttaqi, "A novel control strategy for a variable-speed wind turbine with a permanent-magnet synchronous generator," *IEEE Trans. Ind. Appl.*, vol. 46, no. 1, pp. 331–339, Jan./Feb. 2010.
[7] F. E. Tahiri, K. Chikh, and M. Khafallah, "Designing a fuzzy-PI controller of a stand-alone wind energy conversion system for MPPT," *Innovations in Smart Cities Applications Edition 2*. Cham, Switzerland: Springer, 2019.
[8] Y. Errami, M. Hilal, M. Benchagra, M. Maaroufi, and M. Ouassaid, "Nonlinear control of MPPT and grid connected for wind power generation systems based on the PMSG," in *Proc. Int. Conf. Multimedia Comput. Syst.*, May 2012, pp. 1055–1060.
[9] H. Polinder, F. F. A. van der Pijl, G.-J. de Vilder, and P. J. Tavner, "Comparison of direct-drive and geared generator concepts for wind turbines," *IEEE Trans. Energy Convers.*, vol. 21, no. 3, pp. 725–733, Sep. 2006.

[10] J. Yan, H. Lin, Y. Feng, and Z. Q. Zhu, "Control of a grid-connected direct-drive wind energy conversion system," *Renew. Energy*, vol. 66, pp. 371–380, Jun. 2014.
[11] M. Chinchilla, S. Arnaltes, and J. C. Burgos, "Control of permanent-magnet generators applied to variable-speed wind-energy systems connected to the grid," *IEEE Trans. Energy Convers.*, vol. 21, no. 1, pp. 130–135, Mar. 2006.
[12] I. Munteanu, S. Bacha, A. I. Bratcu, J. Guiraud, and D. Roye, "Energy-reliability optimization of wind energy conversion systems by sliding mode control," *IEEE Trans. Energy Convers.*, vol. 23, no. 3, pp. 975–985, Sep. 2008.
[13] Y. Yang, K.-T. Mok, S.-C. Tan, and S. Y. R. Hui, "Nonlinear dynamic power tracking of low-power wind energy conversion system," *IEEE Trans. Power Electron.*, vol. 30, no. 9, pp. 5223–5236, Sep. 2015.
[14] B. Zigmund, A. A. Terlizzi, X. del Toro García, R. Pavlanin, and L. Salvatore, "Experimental evaluation of pi tuning techniques for field oriented control of permanent magnet synchronous motors," *Adv. Electr. Electron. Eng.*, vol. 5, pp. 114–119, Jun. 2011.
[15] K. G. Papadopoulos and N. I. Margaris, "Extending the symmetrical optimum criterion to the design of PID type-p control loops," *J. Process Control*, vol. 22, no. 1, pp. 11–25, Jan. 2012.
[16] T. Hagglund, *PID Controllers: Theory, Design, Tuning*. 2nd ed. NC, USA: The Instrumentation, Systems, and Automation Society, 1995.
[17] S. M. Tripathi, A. N. Tiwari, and D. Singh, "Optimum design of proportional-integral controllers in grid-integrated PMSG-based wind energy conversion system," *Int. Trans. Electr. Energy Syst.*, vol. 26, no. 5, pp. 1006–1031, May 2016.
[18] Y.-S. Kim, I.-Y. Chung, and S.-I. Moon, "Tuning of the PI controller parameters of a PMSG wind turbine to improve control performance under various wind speeds," *Energies*, vol. 8, no. 2, pp. 1406–1425, Feb. 2015.
[19] M. Alizadeh and S. S. Kojori, "Augmenting effectiveness of control loops of a PMSG (permanent magnet synchronous generator) based wind energy conversion system by a virtually adaptive PI (proportional integral) controller," *Energy*, vol. 91, pp. 610–629, Nov. 2015.
[20] L. Pan and C. Shao, "Wind energy conversion systems analysis of PMSG on offshore wind turbine using improved SMC and extended state observer," *Renew. Energy*, vol. 161, pp. 149–161, Dec. 2020.
[21] M. Jingfeng, W. Aihua, W. Guoqing, and Z. Xudong, "Maximum power point tracking in variable speed wind turbine system via optimal torque sliding mode control strategy," in *Proc. 34th Chin. Control Conf. (CCC)*, Jul. 2015, pp. 7967–7971.
[22] R. Saravanakumar and A. Jain, "Design of complementary sliding mode control for variable speed wind turbine," in *Proc. 8th Int. Conf. Power Energy Syst. (ICPES)*, Dec. 2018, pp. 171–175.
[23] B. Beltran, T. Ahmed-Ali, and M. E. H. Benbouzid, "Sliding mode power control of variable-speed wind energy conversion systems," *IEEE Trans. Energy Convers.*, vol. 23, no. 2, pp. 551–558, Jun. 2008.
[24] A. Merabet, K. T. Ahmed, H. Ibrahim, and R. Beguenane, "Implementation of sliding mode control system for generator and grid sides control of wind energy conversion system," *IEEE Trans. Sustain. Energy*, vol. 7, no. 3, pp. 1327–1335, Jul. 2016.
[25] P. Li, L. Xiong, F. Wu, M. Ma, and J. Wang, "Sliding mode controller based on feedback linearization for damping of sub-synchronous control interaction in DFIG-based wind power plants," *Int. J. Elect. Power Energy Syst.*, vol. 107, pp. 239–250, May 2019.
[26] L. Meegahapola, M. Datta, I. Nutkani, and J. Conroy, "Role of fault ride-through strategies for power grids with 100% power electronic-interfaced distributed renewable energy resources," *WIREs Energy Environ.*, vol. 7, no. 4, Jul. 2018.
[27] K. H. Oon, C. Tan, A. H. A. Bakar, H. S. Che, H. Mokhlis, and H. A. Illias, "Establishment of fault current characteristics for solar photovoltaic generator considering low voltage ride through and reactive current injection requirement," *Renew. Sustain. Energy Rev.*, vol. 92, pp. 478–488, Sep. 2018.
[28] A. Q. Al-Shetwi, M. A. Hannan, K. P. Jern, M. Mansur, and T. M. I. Mahlia, "Grid-connected renewable energy sources: Review of the recent integration requirements and control methods," *J. Cleaner Prod.*, vol. 253, Apr. 2020, Art. no. 119831.
[29] M. K. Dösoğlu and A. B. Arsoy, "Transient modeling and analysis of a DFIG based wind farm with supercapacitor energy storage," *Int. J. Electr. Power Energy Syst.*, vol. 78, pp. 414–421, Jun. 2016.
[30] Y.-W. Shen, D.-P. Ke, W. Qiao, Y.-Z. Sun, D. S. Kirschen, and C. Wei, "Transient reconfiguration and coordinated control for power converters to enhance the LVRT of a DFIG wind turbine with an energy storage device," *IEEE Trans. Energy Convers.*, vol. 30, no. 4, pp. 1679–1690, Dec. 2015.
[31] S. G. Liasi, Z. Afshar, M. J. Harandi, and S. S. Kojori, "An improved control strategy for DVR in order to achieve both LVRT and HVRT in DFIG wind turbine," in *Proc. Int. Conf. Expo. Electr. Power Eng. (EPE)*, Oct. 2018, pp. 0724–0730.
[32] Y. Wang, J. Meng, X. Zhang, and L. Xu, "Control of PMSG-based wind turbines for system inertial response and power oscillation damping," *IEEE Trans. Sustain. Energy*, vol. 6, no. 2, pp. 565–574, Apr. 2015.
[33] N. P. W. Strachan and D. Jovcic, "Stability of a variable-speed permanent magnet wind generator with weak AC grids," *IEEE Trans. Power Del.*, vol. 25, no. 4, pp. 2779–2788, Oct. 2010.
[34] C. Bajracharya, M. Molinas, J. A. Suul, and T. M. Undeland, "Understanding of tuning techniques of converter controllers for VSC-HVDC," in *Proc. NORPIE*, Helsinki, Finland, 2008, pp. 1–8.
[35] J. W. Umland and M. Safiuddin, "Magnitude and symmetric optimum criterion for the design of linear control systems: What is it and how does it compare with the others?" *IEEE Trans. Ind. Appl.*, vol. 26, no. 3, pp. 489–497, May/Jun. 1990.
[36] A. A. A. Radwan and Y. A.-R.-I. Mohamed, "Grid-connected wind-solar cogeneration using back-to-back voltage-source converters," *IEEE Trans. Sustain. Energy*, vol. 11, no. 1, pp. 315–325, Jan. 2020.
[37] A. Yazdani and R. Iravani, *Voltage-Sourced Converters in Power Systems: Modeling, Control, and Applications*. Hoboken, NJ, USA: Wiley, 2010.
[38] V. Yaramasu and B. Wu, *Model Predictive Control of Wind Energy Conversion Systems*. Hoboken, NJ, USA: Wiley, 2016.
[39] F. Blaabjerg, *Control of Power Electronic Converters and Systems*. Cambridge, U.K.: Academic, 2018.
[40] S. M. Mozayan, M. Saad, H. Vahedi, H. Fortin-Blanchette, and M. Soltani, "Sliding mode control of PMSG wind turbine based on enhanced exponential reaching law," *IEEE Trans. Ind. Electron.*, vol. 63, no. 10, pp. 6148–6159, Oct. 2016.
[41] R. Peña-Alzola, M. Liserre, F. Blaabjerg, M. Ordonez, and Y. Yang, "LCL-filter design for robust active damping in grid-connected converters," *IEEE Trans. Ind. Informat.*, vol. 10, no. 4, pp. 2192–2203, Nov. 2014.
[42] R. Peña-Alzola, M. Liserre, F. Blaabjerg, R. Sebastián, J. Dannehl, and F. W. Fuchs, "Systematic design of the lead-lag network method for active damping in LCL-filter based three phase converters," *IEEE Trans. Ind. Informat.*, vol. 10, no. 1, pp. 43–52, Feb. 2014.

AHMED M. OSMAN (Graduate Student Member, IEEE) received the B.E. degree in electrical engineering from the Sudan University of Science and Technology, in 2012. He is currently pursuing the master's degree in electrical engineering with King Abdulaziz University.

He worked as a Teaching Assistant (Tutor) with the Department of Electrical Engineering, Sudan University of Science and Technology, from 2013 to 2016. During 2016–2020, he worked as a Control and Instrumentation Engineer with Sudanese Thermal Power Generating Company. His research interests include integration of renewable energy sources into the grid, control and operation of power plants, and application of modern control techniques in power systems.

FAHAD ALSOKHIRY (Senior Member, IEEE) received the B.Sc. degree (Hons.) in power engineering and electrical machines from King Abdulaziz University, Jeddah, Saudi Arabia, in 2007, and the M.Sc. degree in electrical power engineering with business and the Ph.D. degree in electrical engineering from the University of Strathclyde, Glasgow, U.K., in 2010 and 2016, respectively.

He is currently an Associate Professor with the Electrical and Computer Engineering Department, King Abdulaziz University. He has received research funding as a Principal Investigator on several research projects funded by the Ministry of Education, King Abdullah City for Atomic and Renewable Energy (KACARE) and King Abdulaziz University. His research interests include HVDC systems, multilevel converters, distributed generation, renewable energy generation, grid integration, and smart grids. He is a member of the IEEE Power & Energy and Power Electronics Societies and a member of the IET.